NOTICE

This report was prepared by the State University of New York at Buffalo as a result of research sponsored by the National Center for Earthquake Engineering Research (NCEER) through grants from the National Science Foundation, the New York State Science and Technology Foundation, and other sponsors. Neither NCEER, associates of NCEER, its sponsors, the State University of New York at Buffalo, nor any person acting on their behalf:

a. makes any warranty, express or implied, with respect to the use of any information, apparatus, method, or process disclosed in this report or that such use may not infringe upon privately owned rights; or

b. assumes any liabilities of whatsoever kind with respect to the use of, or the damage resulting from the use of, any information, apparatus, method or process disclosed in this report.

Any opinions, findings, and conclusions or recommendations expressed in this publication are those of the author(s) and do not necessarily reflect the views of NCEER, the National Science Foundation, the New York State Science and Technology Foundation, or other sponsors.

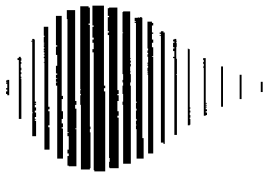

Shape Memory Structural Dampers: Material Properties, Design and Seismic Testing

by

P.R. Witting[1] and F.A. Cozzarelli[2]

May 26, 1992

Technical Report NCEER-92-0013

NCEER Project Number 90-2103

NSF Master Contract Number BCS 90-25010
and
NYSSTF Grant Number NEC-91029

1 Graduate Student, Department of Mechanical and Aerospace Engineering, State University of New York at Buffalo
2 Professor, Department of Mechanical and Aerospace Engineering, State University of New York at Buffalo

NATIONAL CENTER FOR EARTHQUAKE ENGINEERING RESEARCH
State University of New York at Buffalo
Red Jacket Quadrangle, Buffalo, NY 14261

PREFACE

The National Center for Earthquake Engineering Research (NCEER) was established to expand and disseminate knowledge about earthquakes, improve earthquake-resistant design, and implement seismic hazard mitigation procedures to minimize loss of lives and property. The emphasis is on structures in the eastern and central United States and lifelines throughout the country that are found in zones of low, moderate, and high seismicity.

NCEER's research and implementation plan in years six through ten (1991-1996) comprises four interlocked elements, as shown in the figure below. Element I, Basic Research, is carried out to support projects in the Applied Research area. Element II, Applied Research, is the major focus of work for years six through ten. Element III, Demonstration Projects, have been planned to support Applied Research projects, and will be either case studies or regional studies. Element IV, Implementation, will result from activity in the four Applied Research projects, and from Demonstration Projects.

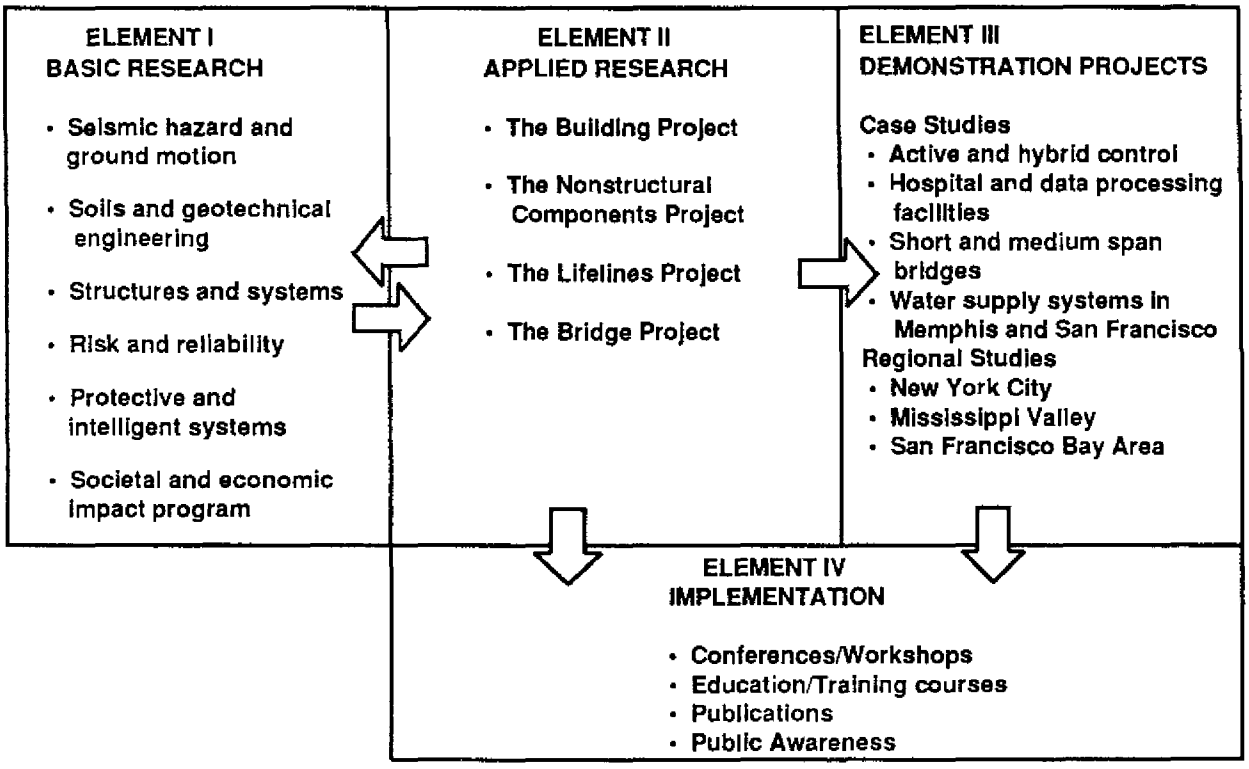

Research in the **Building Project** focuses on the evaluation and retrofit of buildings in regions of moderate seismicity. Emphasis is on lightly reinforced concrete buildings, steel semi-rigid frames, and masonry walls or infills. The research involves small- and medium-scale shake table tests and full-scale component tests at several institutions. In a parallel effort, analytical models and computer programs are being developed to aid in the prediction of the response of these buildings to various types of ground motion.

Two of the short-term products of the **Building Project** will be a monograph on the evaluation of lightly reinforced concrete buildings and a state-of-the-art report on unreinforced masonry.

The **protective and intelligent systems program** constitutes one of the important areas of research in the **Building Project.** Current tasks include the following:

1. Evaluate the performance of full-scale active bracing and active mass dampers already in place in terms of performance, power requirements, maintenance, reliability and cost.
2. Compare passive and active control strategies in terms of structural type, degree of effectiveness, cost and long-term reliability.
3. Perform fundamental studies of hybrid control.
4. Develop and test hybrid control systems.

One of the passive energy dissipation devices studied at NCEER is made of shape memory alloys. The basic idea behind the use of shape memory structural dampers in a structure is to take advantage of the superelastic material properties of shape memory alloys so that significant damping effect can be achieved, while a centering force can be generated to restore the structure to its original position after an earthquake.

This report describes the design, fabrication, and laboratory testing of a class of shape memory structural dampers. Their performance, when added to a 2/5-scale model structure, is compared with that achieved by using traditional viscoelastic dampers.

ABSTRACT

The results of material tests on the shape memory alloy Cu-Zn-Al are presented and discussed. The results of the material tests are then applied in the design of a structural damper, with Cu-Zn-Al providing the dominant damping force. Different damping designs are examined to determine the best design. The finalized design was then mechanically tested.

Seismic response characteristics of a 2/5 model five story building, with and without added Cu-Zn-Al shape memory dampers are studied experimentally. These results are then compared with the studies of viscoelastic dampers tested on the same model five story building.

ACKNOWLEDGEMENT

The funding support granted to the authors by the NCEER is gratefully acknowledged. The authors also gratefully acknowledge the help of Dr. L. McDonald Schetky and Dr. Wu of Memry Metals Inc. Both have provided valuable recommendations on the development of the material experimental program. Also, the authors wish to thank Dr. K.C. Chang for his help with the seismic experimental testing.

TABLE OF CONTENTS

LIST OF ILLUSTRATIONS

LIST OF TABLES

SECTION 1

INTRODUCTION

The use of structural dampers and base isolators have been shown to greatly reduce the damage to a structure due to an earthquake [5,9,11,12]. The study of these devices is somewhat limited, in terms of the material used in the structural dampers and base isolator devices. Viscoelastic structural dampers have been studied in [5,9], and frictional structural dampers were studied in [10,11]. Rubber bearing base isolation devices have also been studied. These are, however, only a few of the many materials which may be used to create the vibration control desired during an earthquake. The emphasis in this study is to research the possible benefits, to passive structural vibration control techniques, of the relatively new class of materials, the shape memory alloy.

Constitutive relation for the shape memory alloy (SMA) have been developed in [13]. In addition, the material properties of a few different shape memory alloys are explored in [7,12]. The objectives of this study were to design, build and test a structural damper which uses a shape memory alloy. The testing of the SMA damper included a study of the dynamic response of a 2/5 scale five-story steel frame structure with added SMA dampers. These results were then compared to viscoelastic dampers, which were tested on the same structure.

SECTION 2

MATERIAL CONSIDERATIONS

2.1 Pseudoelasticity

A shape memory alloy (SMA) undergoes a reversible phase transformation or phase reorientation when deformed. In addition, the SMA can undergo a reversible change in geometry with a change in temperature, which is due to a phase transformation. Pseudoelasticity is the constitutive behavior which describes the above mentioned phenomena. In this study, however, we will only be concerned with stress induced pseudoelastic behavior.

There are two different classes of stress induced pseudoelastic behavior: large area hysteretic behavior and superelasticity. The difference between the two is due to differing A_f and M_f temperatures. The M_f temperature is the temperature below which the alloy has a body centered tetragonal (BCT) martensitic crystal structure. Conversely, above the A_f temperature the alloy has a body centered cubic (BCC) austenitic crystal structure. It should be pointed out that $A_f > M_f$. In addition, if the material temperature falls between A_f and M_f the material will have a mixture of both BCC and BCT crystal structures.

If a SMA at a temperature below its M_f temperature is cyclicly loaded, a large area hysteresis loop is formed. This hysteresis loop, however, is not formed by the dislocation glide mechanism typical of a plastically deforming metal. This loop is due to the growth, shrinkage and rotation of the martensitic crystals. This

allows the SMA to undergo many more large strain high damping cycles than a typical plastically deforming metal. In addition to resistance to large strain fatigue, the material reverts back to the original crystal orientation and therefore to its original shape, if the temperature is raised above the A_f temperature. Thus the material exhibits a shape memory effect.

The superelastic constitutive model describes the stress-strain relation of a SMA at a temperature above the A_f temperature. At low stress levels, a material with superelastic properties will behave elastically. However, at some higher stress level, which depends on the material and its heat treatment, a phase transformation from BCC to BCT begins. This transformation will reduce the modulus of the material as seen in Fig. 2.1. Upon unloading, the material undergoes a reverse transformation at a lower stress level. The difference in the transformation stress level between loading and unloading is due to internal friction in the diffusionless phase transformation. Once the reverse phase transformation is complete, the material behaves elastically, and with complete unloading of the material, a complete recovery is ideally seen. The complete cycle is shown in Fig. 2.1.

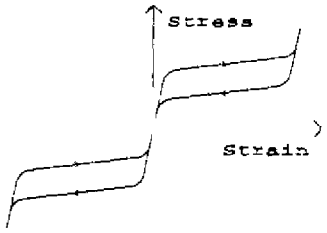

Fig. 2-1 Superelastic Stress Strain Relationship

2.2 Material Selection

Initially this project began by using the SMA nitinal to verify the proposed superelastic constitutive law in [6,16]. While nitinal has very good SMA material properties, it is extremely difficult to machine. Because nitinal is hard and highly abrasive, it requires special tools for machining and thus some machining operations are impractical [6,16]. In addition, nitinal's high cost inhibits its use. Therefore a considerably less expensive shape memory alloy (Cu-Zn-Al) was selected. In addition to its attractive low cost, the machining of this alloy required no special tools and could be completed relatively quickly.

2.3 Cu-Zn-Al Phases and Heat Treatment

The composition of Cu-Zn-Al by weight percent used in this study was 69.1% Cu, 26.9% Zn, 3.75% Al, and 0.1% Zr. This composition of Cu-Zn-Al, in equilibrium at room temperature, has two phases α and γ. The α phase is the copper FCC structure, and the γ phase is an intermediate compound with the composition of Cu_5Zn_8. Above 725°C, the Cu-Zn-Al is in the β phase which has a BBC structure. Just below 725°C, the equilibrium phases are β and α. The γ phase appears below 300°C and has much slower kinetics [14]. Even with a moderately slow cool to room temperature, only the α and β phases would be present.

Since the tensile bars were machined from a 3 inch diameter bar of Cu-Zn-Al, considerable machining was necessary. This machining heats up the material significantly. To prevent the

problem of the machining process annealing the heat treatment, the Cu-Zn-Al SMA was heat treated after the machining process was complete.

The heat treatment began by heating the Cu-Zn-Al SMA in an argon bath at 800°C for 30 minutes, which is then followed by a water quench. At 800°C the microstructure of Cu-Zn-Al is the single phase β. Immediately after the water quench, the Cu-Zn-Al is aged at 80°C for 24 hours. The argon bath was used to prevent nitrogen embrittlement, and reduce dezincification during the high temperature part of the heat treatment [15]. Since the second part of the heat treatment is at a much lower temperature, it was performed without an argon bath. The water quench from 800°C prevents the Cu+Zn-Al from transforming from the β phase, however the martensitic transformation temperature of this as-quenched single β phase is unstable. The aging at 80°C allows the short range order of the β phase to reorient to a more stable form [7]. Despite the use of the argon gas to prevent extensive damage to the surface of the specimen during heat treatment, the surface still needed hand sanding to remove some damaged surface without heating up the material.

2.4 Material Testing

Tensile and differential scanning calorimeter (DSC) tests were performed to verify the A_f and M_f temperatures as well as the superelastic properties. The DSC tests were performed at Memry Technologies Inc. by Dr. Wu.

A Mechanical Testing System (MTS) machine was used to perform the mechanical tests. This MTS machine was configured to use feedback control of strain to produce a ramp strain loading on the sample. The strain was measured with a model 11B-20 MTS extensometer. This extensometer measures the average strain over an one inch region. An OPTILOG data acquisition system, which was connected to a PC, was used to convert the voltage signals from the MTS load cell, displacement transducer and extensometer to mechanical measurements, which could be stored on computer disk.

The tensile bars used in the mechanical testing were designed to undergo both tensile and compressive loads without bucking. Appendix B contains drawings of both the tensile bar and the grip design. Sample bar D was heat treated then tested under strain controlled conditions to a maximum strain of .1% strain to determine the elastic modulus. The elastic modulus was found to be 7.2×10^6 Psi. Sample bar A was heat treated then tested under strain controlled conditions to a maximum strain of 2.2%. Six tension compression cycles were performed. The resulting stress-strain curve is presented in Fig. 2.2. The initial elastic modulus of the first cycle of the stress strain curve was 7.6×10^6 Psi. At .25% strain the modulus begins to drop and at 1.00% strain it has leveled out at 5.8×10^5 Psi. The maximum tensile strain was 2.22% under a load of 34.8 Ksi. A plastic constitutive law would predict that the remaining strain after unloading would be 1.76%. The remaining strain was .26% which indicates a 1.50% strain springback.

The first cycle of the stress strain curve has a much more pronounced superelastic characteristic than the subsequent cycles. Notice in Fig. 2.2 that the loading of the first compressive load show a pronounced softening of modulus at -.25% strain. The second compressive cycle has a less pronounced softening of modulus at -.7% strain. This softening of modulus all but disappears after the 3rd cycle. The overall appearance of the 3rd and subsequent cycles is of a slightly hour-glass-shaped hysteresis loop. The local modulus of the Cu-Zn-Al after several cycles is 3.3×10^6 on initial unloading of the stress. This is much less then the elastic modulus measured. In addition, the modulus reduces during the unloading to 2.2×10^6 Psi. If the Cu-Zn-Al were deforming though dislocation slip/glide mechanisms, then these moduli would be equal to the elastic modulus.

The test was repeated on sample bar C with the same heat treatment and the results were similar. These results are presented in Fig. 2.3.

Heat Treatment: 800°C 30 min (Argon) W.Q.

: 80°C 24 hours (Air)

ε Limits: -0.022/0.022 (Rate=.000077/sec)

Test Section Diameter D = 0.496 in

Extensometer Gage Length: L = 1.0 in

6 Cycles

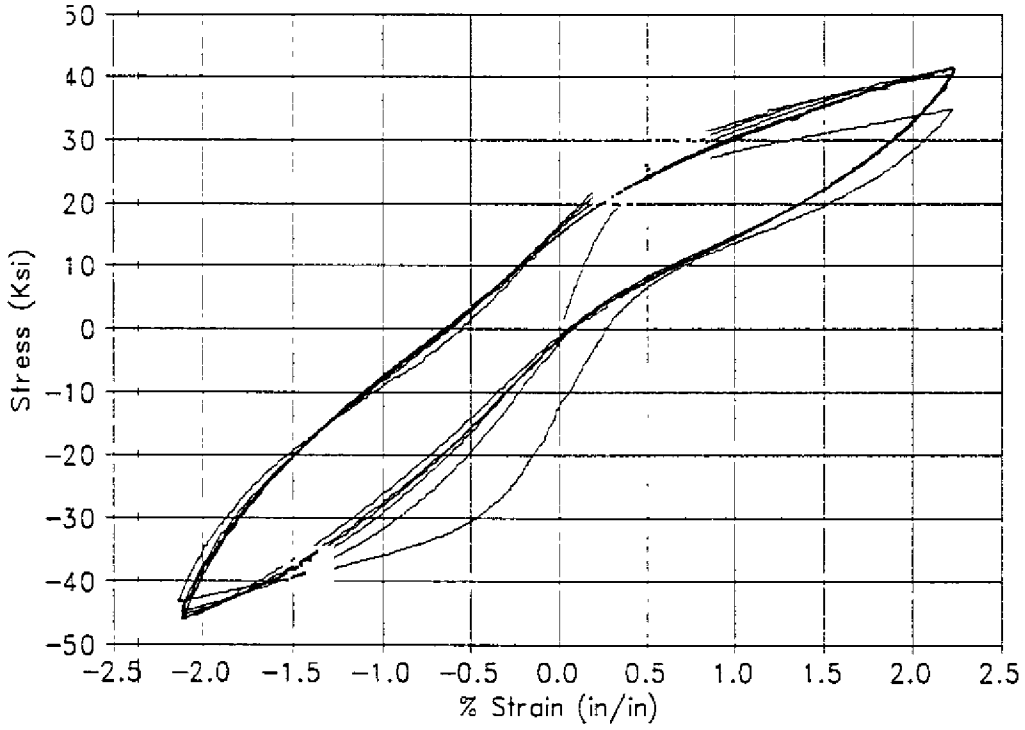

Fig. 2-2 Six Cycle test of heat treated Cu-Zn-Al, Bar A

Heat Treatment: 800°C 30 min (Argon) W.Q.

: 80°C 24 hours (Air)

ε Limits: -0.020/0.020 (Rate=.000382/sec)

Test Section Diameter D = 0.485 in

Extensometer Gage Length: L = 1.0 in

6 Cycles

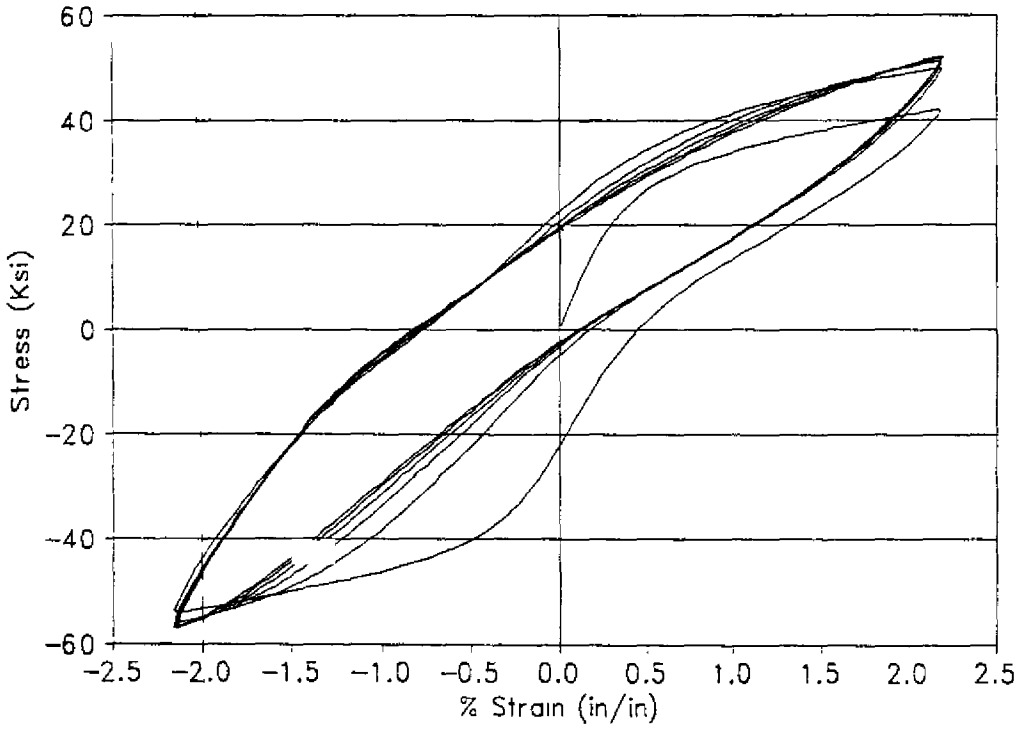

Fig. 2-3 Six Cycle test of heat treated Cu-Zn-Al, Bar C

A DSC test was performed on a sample of the strained section of bar A. A DSC was also performed on a unstrained heat treated sample of the Cu-Zn-Al for comparison. Table 2.1 presents the results of these tests.

DSC Test Results	Heat treated Unstrained	Heat treated Strained Bar A
Δh for BCC to BCT phase transformation	-0.86 cal/gram	-0.34 cal/gram
Δh for BCT to BCC phase transformation	1.21 cal/gram	0.87 cal/gram
Onset temperature of BCC to BCT phase transformation	-8°C	-15°C
Completion temperature of BCC to BCT phase transformation	-30°C	-52°C
Onset temperature of BCT to BCC phase transformation	-12°C	-23°C
Completion temperature of BCT to BCC phase transformation	8°C	1°C

Table 2-I DSC Results of Strained and Unstrained Cu-Zn-Al

The onset and completion temperatures are lower for the strained bar, and the total temperature range in which the phase transformation takes place is wider for the strained sample. In addition, the magnitude of the enthalpy change (Δh) for both phase transformations is smaller in the strained sample.

It should be noted that the magnitude of the enthalpy change for the BCC to BCT phase transformation is smaller than the magnitude for the BCT to BCC transformation. If the transformations were thermodynamically reversible, the magnitudes

of the enthalpy changes would be identical. However this is not the case with Cu-Zn-Al. Frictional energy is lost during a martensitic transformation. This frictional energy will always contribute a positive term to the enthalpy change. The BCC to BCT transformation is endothermic, and will produce a negative enthalpy change. The BCT to BCC phase transformation is exothermic, and will produce a positive enthalpy change. The frictional term is added to both of these reactions, which decreases the magnitude of the BCT to BCC enthalpy change and increases the BCC to BCT enthalpy change. If we assume that the frictional energies produced by both the forward and reverse martensitic transformations are the same, then the average of the magnitudes of the enthalpies is the enthalpy associated with phase transformation. With the same assumption, one half the difference of the magnitudes is the enthalpy change due to friction. Thus

$$\Delta h_{pt} = \frac{|\Delta h_{BCT\text{-}BCC}| + |\Delta h_{BCC\text{-}BCT}|}{2}$$
$$\Delta h_{f} = \frac{|\Delta h_{BCT\text{-}BCC}| - |\Delta h_{BCC\text{-}BCT}|}{2} \qquad (2.1)$$

where subscripts pt and f refer to phase transformation and friction respectively.

The Δh_{pt} of the unstrained sample is 1.05 cal/gram, while the Δh_{pt} of the strained sample is 0.61 cal/gram. This indicates that less of the strained sample is transformed. The frictional enthalpy change was calculated as 0.16 cal/gram for the unstrained

sample and 0.26 cal/gram for the strained sample, using Eq. 2.1. Thus the strained sample had a smaller amount of material transformed and a greater amount of friction associated with this transformation.

With the above knowledge of the increased friction of transformation and the decrease in the amount of Cu-Zn-Al transforming, the Stress vs Strain curves of Fig. 2.2 can be explained. The first cycle is the expected superelastic relationship. During this cycle, the dislocations are formed from the phase transformation [17] and the internal friction increases. The increased friction has the effect of widening the interval between the loading and unloading stress strain paths. In Cu-Zn-Al, this widening is large enough to cause a stress strain curve to look like a simple hysteresis loop.

SECTION 3

DAMPER DESIGN

3.1 Requirements of SMA Damper

The essential idea behind the damper design was to create a structural damper that would take advantage of the Cu-Zn-Al superelastic material properties, discussed in Sec. 2, to damp the building's motion and generate a centering force on the building. The purpose of this form of a damper is to minimize the motion of the building during the earthquake, and to restore the building to its original position after the earthquake is over.

A model five story building, built by the joint U.S.-China Cooperative Research Program, was used to test the SMA dampers. The building was designed to allow different dampers to be installed in the cross bracing. The cross bracing is at a 45° angle to the floor as shown in Fig. 3.1.

The dampers had to be designed to satisfy the requirements of the model five story building, on which the earthquake tests were performed. Because the building is used for many tests, the tests must of course not damage the building. To prevent such damage, the maximum inter-story drift was limited to .25 inches. Furthermore, since we did not want to drastically change the natural frequency of the building, the maximum additional inter-story stiffness, due to the presence of the dampers, was set at 9000 lbs/inch maximum.

Along with constraints imposed by the building there were also some material constraints to be considered in the design. The

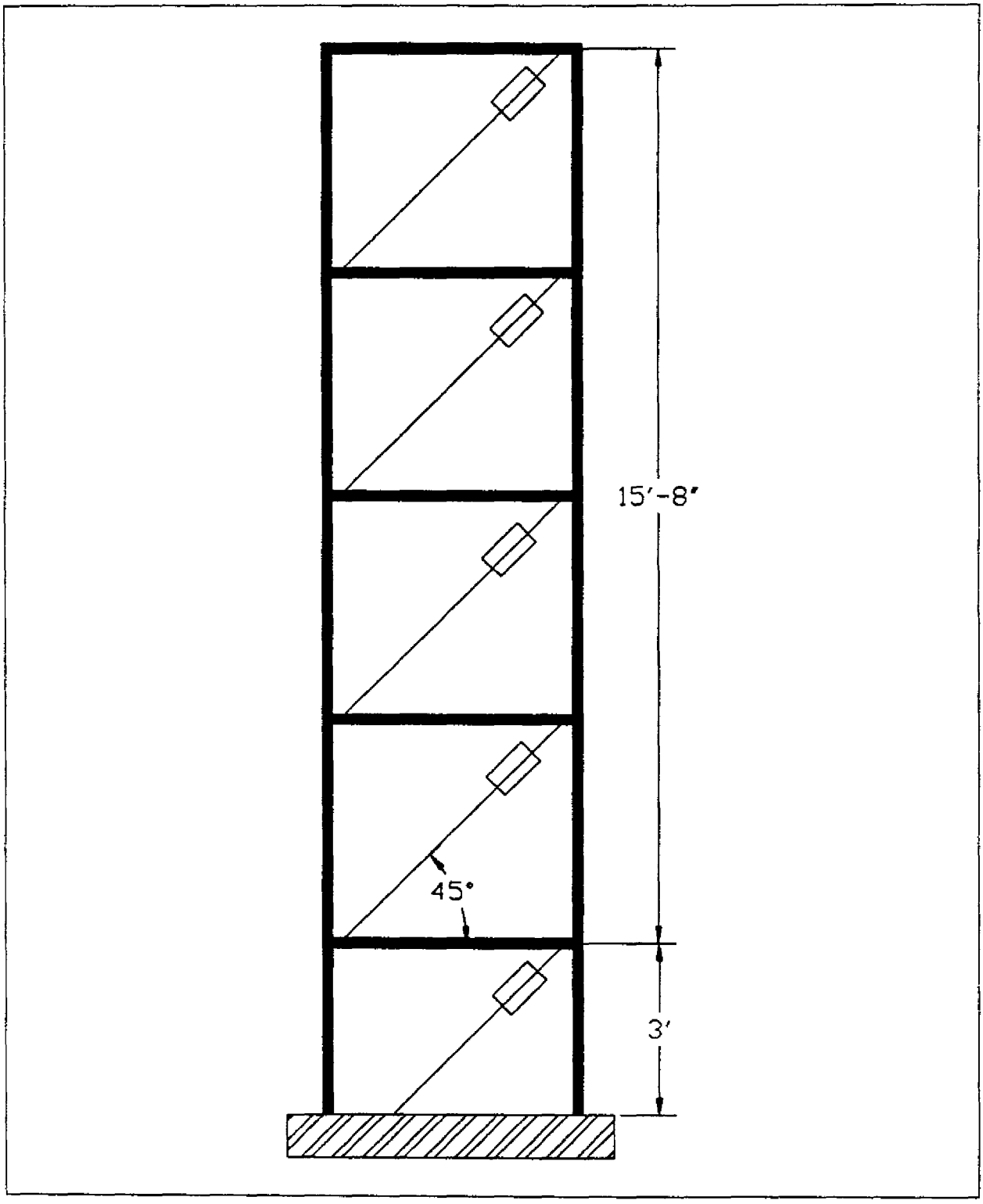

Figure 3-1 Five Story Model building

maximum strain in the Cu-Zn-Al was set at 2% to guarantee that the material would not yield plastically. However the design had to ensure that strains up to this 2% maximum would be induced, because larger energy absorbing shape memory hysteresis loops occur at the high strain levels.

3.2 Selecting Damper Design

Four designs for producing such a damping device using Cu-Zn-Al were investigated. The designs' principal mechanisms were the bar in torsion, beam in bending, axially loaded beam and the clamped plate loaded in the center. In the comparison of these different types of devices, a linear constitutive law was used although it is quite clear from Sec. 2 that a nonlinear model would more accurately predict the behavior. However, it became clear, from the linear analysis to follow, which design would work the best. A nonlinear model was then used to more accurately determine the exact dimensions of the design.

In the following analysis, the shear and Young's moduli were estimated from the tensile tests on Cu-Zn-Al (Sec. 2.4). Young's modulus was taken to be the stress divided by the strain at 2.4% strain. The shear modulus was then taken to be half the Young's modulus. The values gave a rough estimate on the performance of the damper, and was all that was needed to determine which design to use.

The first design considered was the Cu-Zn-Al annular plate clamped at the inside edge and at the outside edge (Fig. 3.2).

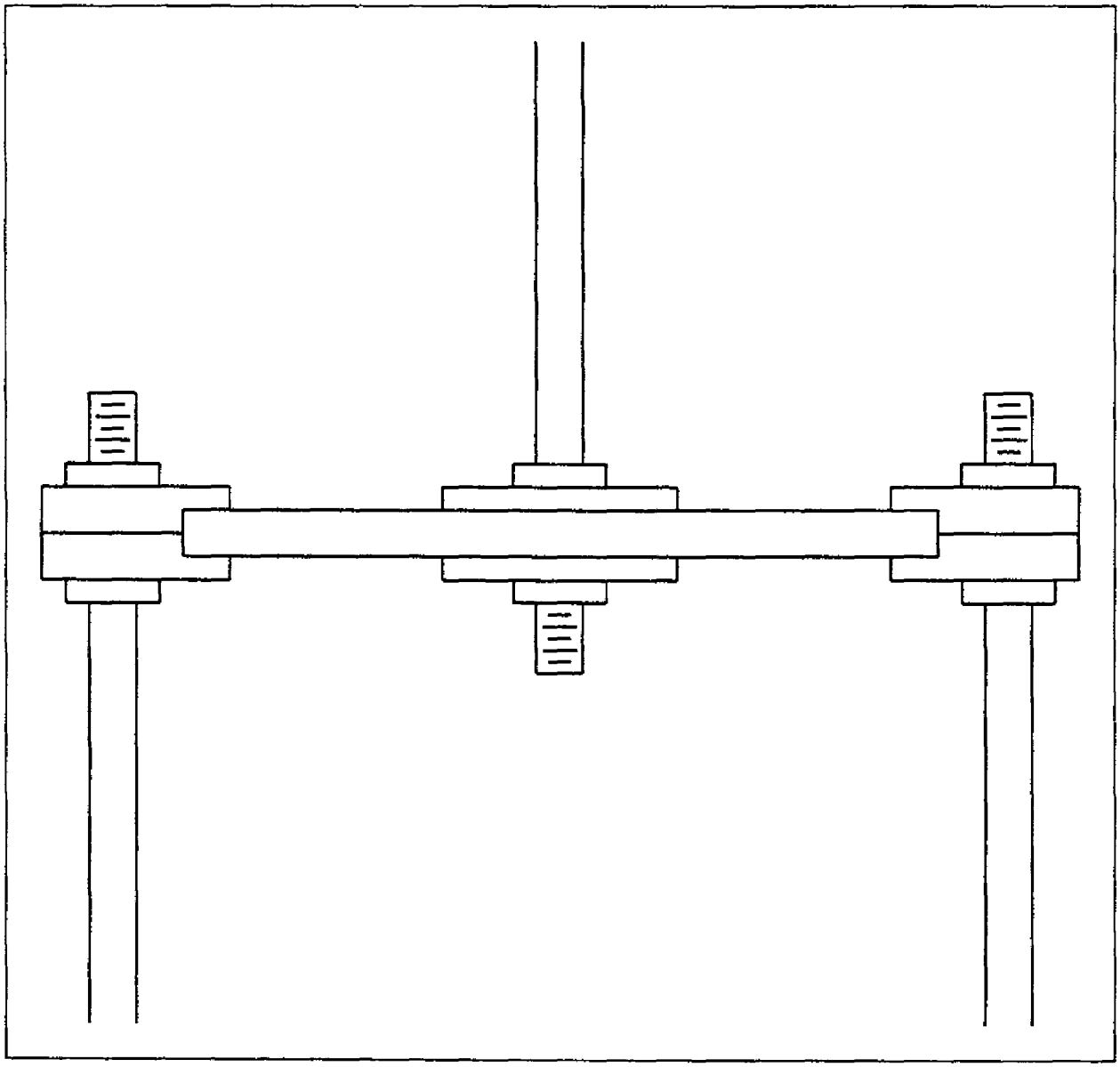

Fig 3-2 Annular Plate

After an examination at the force deflection equation [1], with thicknesses and radii of Cu-Zn-Al washers that were practical to machine, it was found that the idea was much too stiff and resulted in very small strains. The axially loaded beam was also found to be unsuitable, because the constraints of stiffness and strain would cause a beam, made from Cu-Zn-Al with these properties, to buckle.

The torsional bar and bending beam designs both could be made with the suitable stiffness and the desirable strains. Therefore an analysis comparing the two energy absorbing capabilities of the two designs was completed in order to determine which design is best. Since larger strains clearly result in more energy absorbed during cyclic loading (Sec 2), the strain ranges ε_{low} to ε_{max} that contain 90% of the strain energy was compared between the two designs. Below is the development of the analysis for both the bending beam and torsional bar designs.

The bending beam design (Fig. 3.3) is clamped in the middle and at the outside edges. Note that the direction of the deflection of the damper (δ) is in the same direction as the applied force F. The force (F) deflection (δ) equation in terms of the length of the beam (L), width of beam (B), height of beam (H), and modulus of Cu-Zn-Al (E) becomes [1]

$$F = \frac{2EBH^3}{L^3}\delta \qquad (3.1)$$

Due to the constraint of stiffness (S) imposed by the building, we

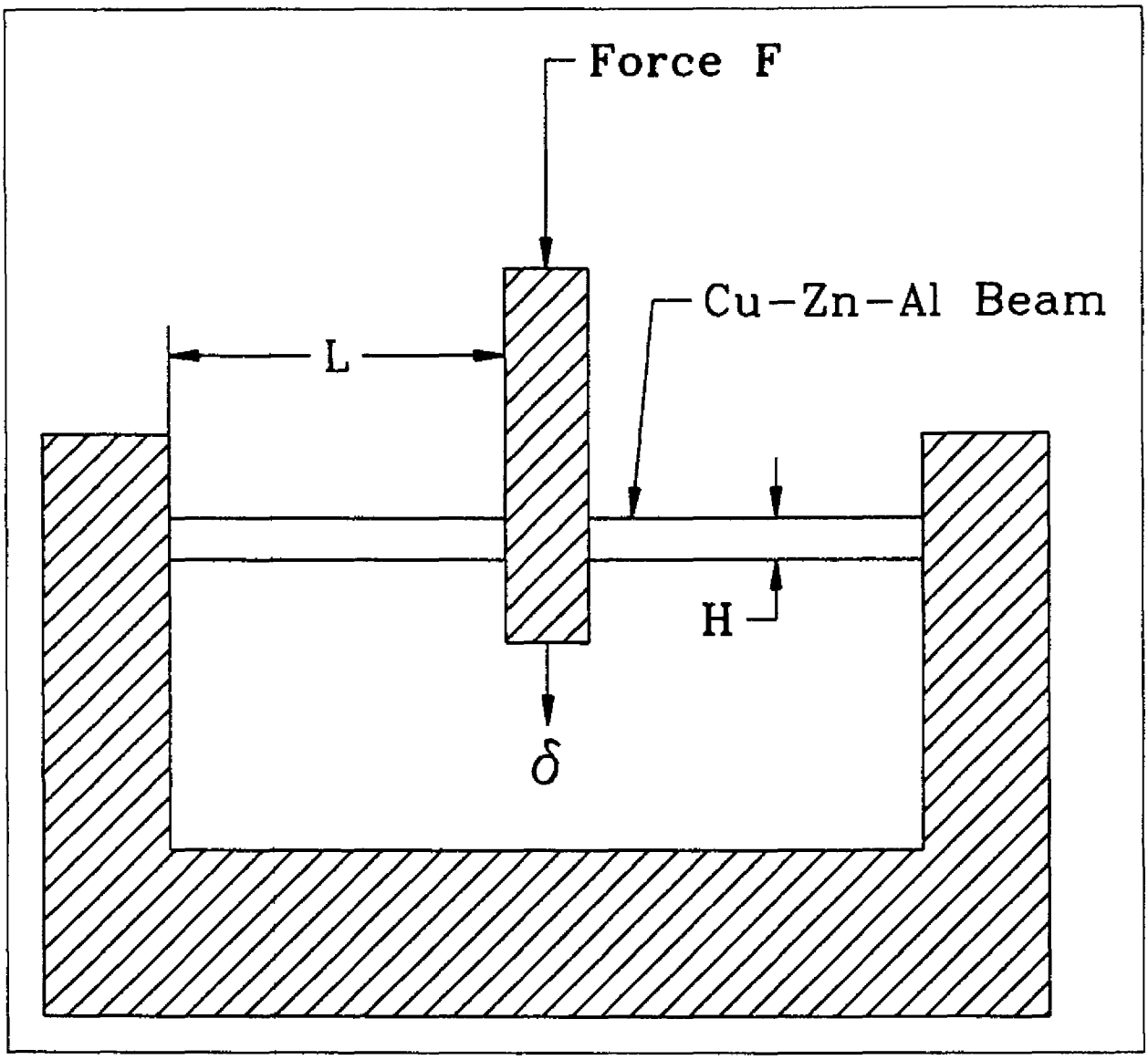

Fig. 3-3 Bending Beam Design

shall ensure the proper stiffness S by setting it to the expression

$$S=\frac{2EBH^3}{L^3} \qquad (3.2)$$

Therefore the force deflection equation reduces to $F=S\delta$. The bending moment equation along the length of the beam [2] is

$$M(X)=\frac{F}{4}[2X-L] \qquad (3.3)$$

Combining the linear elastic constitutive law $\tau=E\varepsilon_{xx}$, the strength of materials flexure formula, and the bending moment equation above, and then solving for the strain yields

$$\epsilon_{xx}=\frac{3Fy}{EBH^3}[2X-L] \qquad (3.4)$$

The maximum strain ε_{max} occurs at x=L, y=H/2, and the maximum force $F=S\Delta$, where Δ is the maximum expected displacement of the damper. Substituting these values in Eq. (3.4) yields

$$\epsilon_{max}=\frac{3LS\Delta}{2EBH^2} \qquad (3.5)$$

Solving Eq. (3.2) and (3.5) for B and H then yields

$$B=\frac{27S\Delta^3}{2E\epsilon_{max}^3L^3} \qquad H=\frac{\epsilon_{max}L^2}{3\Delta} \qquad (3.6)$$

Substituting Eq. (3.6) back into Eq. (3.4) yields

$$\epsilon_{xx}=\frac{6\Delta(2x-L)y}{L^3} \tag{7}$$

Eq. (3.6) and Eq. (3.7) allow the constraints of stiffness (S), maximum strain (ε_{xx}), and maximum deflection (Δ) to be prescribed, so that the height (H) and thickness (B) of the beam becomes a function of L only.

The strain energy density is given by $U_o=\frac{1}{2}E\varepsilon^2_{xx}$. The strain energy function is symmetric in both the horizontal and vertical directions. Therefore, it is necessary to integrate over only one quarter of the beam. However, if only one quarter of the beam is used for integration, the total strain function must be multiplied by eight, since there are two symmetric beams (Fig 3.3) of length L with four sections of symmetry. The integral of the strain energy is thus

$$U=8\int_{x_{min}}^{x_{max}}\int_{y_{min}}^{y_{max}}\int_{z_{min}}^{z_{max}}\frac{1}{2}E\epsilon_{xx}^2\,dz\,dy\,dx \tag{8}$$

In order to integrate over the region of high strain, the limits of integration must be found. The region of high strain shall be defined as the region with strains between ε_{low} and ε_{max}. Since the strain is not a function of the z direction, the limits become $Z_{min}=0$ and $z_{max}=B$. Clearly the end of the beam is the high limit of integration in the x direction thus $x_{max}=L$. The lower limit can be found by substituting into Eq. (3.7) the values $\varepsilon_{xx}=\varepsilon_{low}$ and $y=H/2$, and solving for x. Substituting Eq. (3.6) into the resulting expression yields

$$x_{min}=\frac{L}{4}\left[\frac{\epsilon_{low}}{\epsilon_{max}}+1\right] \tag{3.9}$$

The top of the beam is clearly the max limit in the y direction $y_{max}=H/2$. The lower limit can be found as a function of x by setting $\varepsilon_{xx}=\varepsilon_{low}$ and solving for y. This limit becomes

$$y_{min}=\frac{L^3\epsilon_{low}}{6\Delta(2x-L)} \tag{3.10}$$

The integral over the area of high strain, with appropriate limits, now becomes

$$U=8\int_{\frac{L}{2}\left[\frac{\epsilon_{low}}{\epsilon_{max}}+1\right]}^{L}\int_{\frac{L^3\epsilon_{low}}{6\Delta(2x-L)}}^{\frac{H}{2}}\int_0^B \frac{18\Delta^2E(2x-L)y^2}{L^6}dzdydx \tag{3.11}$$

Integrating and substituting $\beta=\varepsilon_{low}/\varepsilon_{max}$ yields

$$U=\frac{S\Delta^2}{2}\left[1-\beta^3+3\beta^3\ln(\beta)\right] \tag{3.12}$$

If $\varepsilon_{low}=0$ then $\beta=0$ and Eq. (3.12) simplifies to $U=\Delta^2S/2$ which is the total energy of the system.

The strain energy of the torsional bar will now be investigated. The basic dimensions of the damper used in the design are the torsion arm length D, radius of torsion bar R, and length of torsion bar L (Fig. 3.4). Note that the torsion bar length L is defined as the distance between the torsion arm and the side grips as shown in the drawing of the torsional bar design (Fig. 3.4) The torsion arm length is measured from the center of

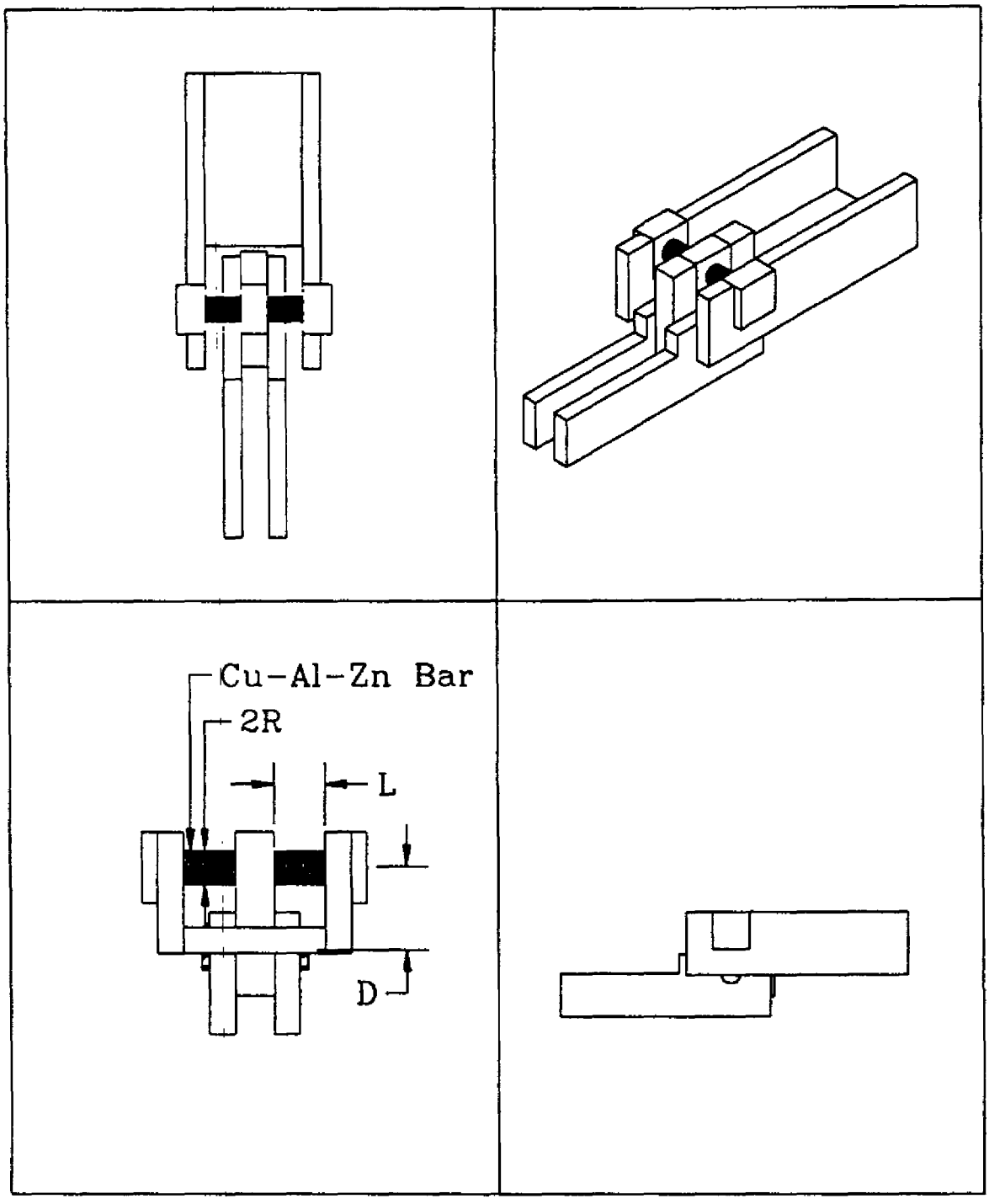

Fig. 3-4 Torsional Bar Design

the torsion arm to the center of the pivot. The displacement δ is again in the same direction as the force F (Fig. 3.4).

From solid mechanics, the angle of twist θ of a solid round bar of radius R and length L with a torque T applied at the end of the bar is

$$\theta = \frac{2TL}{GR^4} \tag{3.13}$$

The angle of twist θ due to the displacement δ is expected to be small, therefore

$$\frac{\delta}{D} = \sin(\theta) \approx \theta \tag{3.14}$$

The equation for shear strain ε_{xy}, in terms of the L, D, δ and the radial distance from the center of the Cu-Zn-Al bar r, is

$$\varepsilon_{xy} = \frac{\theta r}{2L} = \frac{\delta r}{2LD} \tag{3.15}$$

Also, the equation for the force F on the damper in terms of L, D, δ and r is given by

$$F = \frac{\pi G R^4 \delta}{LD^2} \tag{3.16}$$

As before, the stiffness S is defined so that $F = S\delta$, giving

$$S = \frac{\pi G R^4}{LD^2} \tag{3.17}$$

The maximum shear strain occurs at r=R when δ is equal to the maximum deflection allowed (Δ). Substitution into Eq. (3.15) yields

$$\epsilon_{max}=\frac{\Delta R}{2LD} \tag{3.18}$$

Solving Eq. (3.17) and Eq. (3.18) for L and D yields

$$L=\frac{\Delta^2 S}{4\pi GR^2\epsilon_{max}^2}, \qquad D=\frac{2\pi GR^3\epsilon_{max}}{\Delta S} \tag{3.19}$$

Upon substitution of Eq. (3.19) into Eq. (3.15) the following simple expression for shear strain results

$$\epsilon_{xy}=\frac{\epsilon_{max}r}{R} \tag{3.20}$$

The equation for strain energy density is $U_o=2G\varepsilon^2_{xy}$. This equation must be integrated over the high strain region in a manner similar to the procedure used for the bending beam design. The strain is independent of the y and θ directions, so those limits become $y_{min}=0$, $y_{max}=L$, $\theta_{min}=0$ and $\theta_{max}=2\pi$. The maximum limit in the r direction is $r_{max}=R$. The minimum value of r can be found by substituting ε_{low} for ε_{xx} in Eq. (3.20); this limit then becomes $r_{low}=R\varepsilon_{low}/\varepsilon_{max}$. The total strain energy function, after using Eq. (3.19) to eliminate L, finally becomes

$$U=2\int_0^{2\pi}\int_0^{\frac{\Delta^2 S}{4\pi GR^2\epsilon_{max}^2}}\int_{\frac{R\epsilon_{low}}{\epsilon_{max}}}^{R}\frac{2G\epsilon_{low}^2}{R^2}r^3\,dr\,dy\,d\theta \qquad (3.21)$$

Integrating and substituting $\beta=\varepsilon_{low}/\varepsilon_{max}$ yields

$$U=\frac{\Delta^2 S}{2}[1-\beta^4] \qquad (3.22)$$

If $\varepsilon_{low}=0$ then $\beta=0$, and Eq. (3.20) simplifies to $U=\Delta^2 S/2$ which is the total energy put into the system.

The strain energy equations Eq. (3.12) and Eq. (3.22) can be divided by $\Delta^2 S/2$ to yield the percent of the total strain energy $\Delta^2 S/2$ as a function of the strain range β integrated over. Fig. 3-5 is a comparative plot of the percent total strain energy vs the strain range β for the torsional bar and the bending beam designs. It can be seen from Fig. 3-5 that for any given β between 0 and 1 the percent of total strain energy contained within that region is higher for the torsional bar damper design. This means that more of the energy is put into higher strain regions in the torsional bar design than the bending beam design. The larger strain results in a greater amount of energy absorbed, and therefore the torsional bar design apparently results in a more effective damper.

3.3 Final Damper Design

The finalized damper design was determined though analytical and experimental methods. The first damper was designed by employing available analytical tools and material data. This

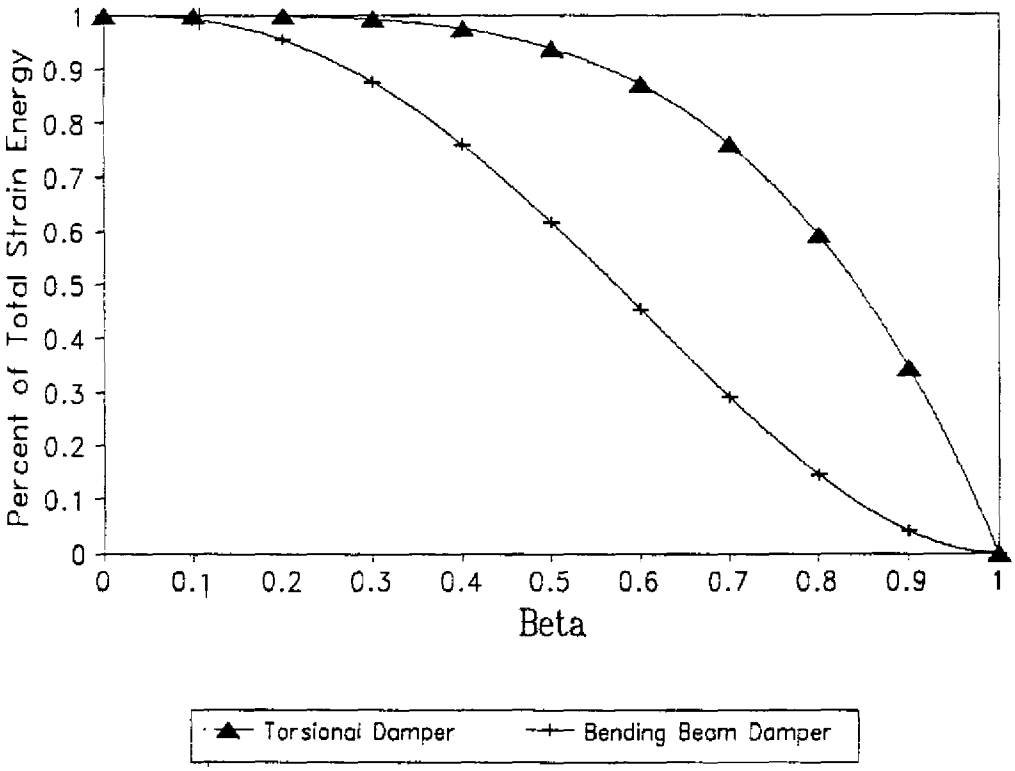

Fig. 3-5 Percent Strain Energy vs Strain Range β

design was then built and tested on the MTS tensile tester. The results were then used to modify the estimated material properties and determine a new design.

After the torsional bar design was chosen, a more accurate nonlinear model for design was developed. The constitutive law used in the analysis was bilinear, i.e.

$$\tau_{xy}=2G_1\epsilon_{xy}+[2(G_1-G_2)(\epsilon_t-\epsilon_{xy})]U(\epsilon_{xy}-\epsilon_t) \qquad (3.23)$$

Notice there are two shear moduli: G_1 which is the elastic shear modulus and G_2 the inelastic shear modulus (see Fig 3.6). Also

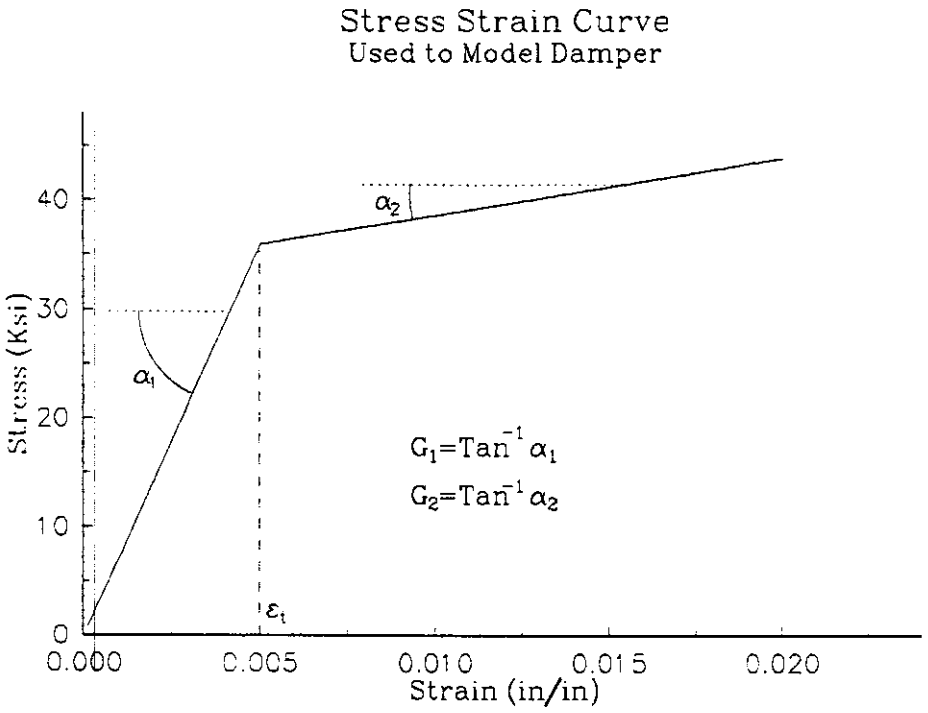

Fig. 3-6 Stress Strain Curve Used to Model Damper.

note from the figure that ε_t is the value of the strain at which the stress strain diagram changes slope. The term $U(\varepsilon_{xy}-\varepsilon_t)$ is a step function and is defined as follows:

$$U(x)=\begin{cases}0 & \text{if } x\le 0\\ 1 & \text{if } x>0\end{cases} \qquad (3.24)$$

The stress strain curve for Eq. (3.23) is given in Fig 3.6.

The torque produced from the two torsional bars in the damper design (Fig. 3.4) is

$$T=FD=2\int_0^{2\pi}\int_0^R(\tau_{xy}r)\,r\,dr\,d\theta \qquad (3.25)$$

Substituting in the constitutive law, Eq. (3.23), and Eq. (3.15) for the shear strain, and solving for the force F gives the following:

$$F=\frac{4}{D}\int_0^{2\pi}\int_0^R\left\{\frac{G_2\delta}{2LD^2}r+[(G_1-G_2)(\varepsilon_t-\frac{\delta}{2LD}r)]U(\varepsilon_{xy}-\varepsilon_t)\right\}r^2\,dr\,d\theta \qquad (3.26)$$

Assuming that $R>2LD\varepsilon_t/\delta$, the integration of Eq. (3.26) simplifies after some manipulation to

$$F=\frac{\pi G_2R^4}{LD^2}\delta+\frac{8\pi\varepsilon_t}{3D}(G_1-G_2)\left[R^3-\frac{2(LD\varepsilon_t)^3}{\delta^3}\right] \qquad (3.27)$$

The above equation gives the force deflection curve for different values of L,D and R. For design, however, we must control the

maximum strain ε_{max} and the stiffness S. The stiffness will now be redefined as the force needed to produce the maximum deflection Δ, divided by Δ. With δ equal to Δ and with S as defined above, Eq. (3.18) and Eq. (3.27) are solved for D and R in terms of L. The results are as follows:

$$D=\left(\frac{3S\Delta^4}{2^4\pi L^3 e_{max}\left[3G_2 e_{max}^4+e_t(G_1-G_2)\left(4e_{max}^3-e_t^3\right)\right]} \right)^{\frac{1}{2}}$$

$$R=\left(\frac{3S\Delta^2 e_{max}}{2^2\pi L\left[3G_2 e_{max}^4+e_t(G_1-G_2)\left(4e_{max}^3-e_t^3\right)\right]} \right)^{\frac{1}{2}} \qquad (3.28)$$

The original damper was designed to err on the stiff side, because the radius of the torsional bar could be turned down on the lathe and then retested until the correct stiffness was achieved. After the first damper was built and tested at different radii, the shear modulus was modified to fit the results of the testing and the final design was determined. A schematic drawing of the damper and the bracing is presented in Appendix A.

It should be noted that in the torsion bar design, the Cu-Zn-Al bar acts as a beam in bending in addition to the desired mechanism of a bar in torsion. Since the Cu-Zn-Al bar is clamped on both ends, the deflection of the Cu-Zn-Al bar due to bending can be modeled as a beam clamped at the ends and loaded at midspan. Using a linear constitutive relationship, the stiffness K of the torsion bar in bending is

The stiffness due to torsion for the same bar is given in Eq. 3.17.

$$K = \frac{6\pi ER^4}{L^3} \qquad (3.29)$$

Dividing Eq. 3.17 by Eq. 3.29 and replacing G with E/(1+ν) gives with a little rearrangement

$$\frac{S}{K} = \frac{1}{6(1+\nu)}\left(\frac{L}{D}\right)^2 \qquad (3.30)$$

To ensure that the deflection of the Cu-Zn-Al bar in bending is insignificant in comparison to the deflection due to the torsion, we set $S/K<0.1$. Assuming $\nu=0.3$, $D>1.13L$ would satisfy the above conditions.

3.4 Cu-Zn-Al Damper Testing

After the damper had been constructed and the Cu-Zn-Al heat treated, the damper was tested on the MTS machine. Fig. 3.6 shows the force deflection relationship of the Cu-Zn-Al torsional bar structural damper. The shape of the force deflection curve changes in a similar fashion to the Cu-Zn-Al stress strain curves in Sec. 2.4. The first cycle of the force deflection curve has a much more pronounced superelastic characteristic than the subsequent cycles.

A comparison between the stiffness and energy loss between the SMA damper and the viscoelastic damper can now be made. The stiffness of the SMA damper was 8813 lb/inch, which was the target stiffness. In addition, the energy loss per cycle was calculated to be 68.1 lb-in. The fourth cycle was used for this calculation since the force deflection curve has stabilized at that cycle. The

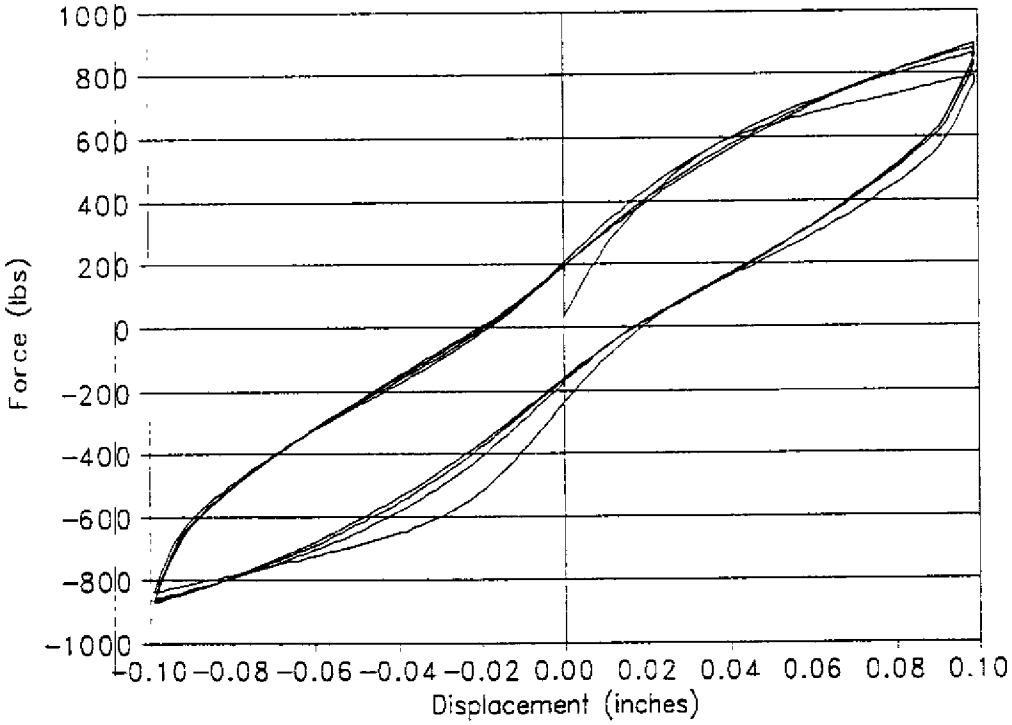

Fig. 3-7 Force vs Disp. of Cu-Zn-Al Damper.

viscoelastic damper's stiffness and energy loss per cycle varied with frequency, temperature and percent strain [5]. At 0.1 Hz, 5% strain and 40°C, the viscoelastic damper had a energy loss per cycle of 69 lb-in and a stiffness of 322 lb/inch. However at 4 Hz, and 20% strain and 21°C, the same viscoelastic damper had a energy loss per cycle of 28431 lb-in and a stiffness of 5311 lb/inch. These results would indicate that the viscoelastic damper would provide greater damping than the SMA damper.

It should be pointed out that while the SMA damper does not provide as much damping as a viscoelastic damper, it can be used in applications where the viscoelastic damper cannot. The three fundamental advantages of a damper designed with SMA material over viscoelastic material are: SMA are much stronger, relatively insensitive to temperature, and it can provide a restoring force. These three factors make SMA materials suitable for a base isolation system. A base isolation system must be strong enough to support the building and should restore the building back to its original position after an earthquake. The viscoelastic damper could not be used for this purpose since the material is much to soft to support this type of load.